

Analysis of the electrical transport, conductivity and dielectric relaxation behavior of $\text{La}_{0.75}\text{Ba}_{0.10}\text{Sr}_{0.15}\text{FeO}_{2.875-\delta}$ ($\delta = 0.375$ and 0.50) brownmillerite oxides

Mariam Bouzayen (✉ maryemmr2@gmail.com)

University of Sfax: Universite de Sfax <https://orcid.org/0000-0002-0652-9445>

Radhia Dhahri

Universite de Sfax Faculte des Sciences de Sfax

Meriem Saadi

University of Gabes Faculty of Sciences of Gabes: Universite de Gabes Faculte des Sciences de Gabes

Slaheddine Chaabouni

Universite de Sfax Faculte des Sciences de Sfax

Kamel Khirouni

University of Gabes Faculty of Sciences of Gabes: Universite de Gabes Faculte des Sciences de Gabes

B F O Costa

University of Coimbra: Universidade de Coimbra

Research Article

Keywords: brownmillerite, ionic and electronic conductivity, oxygen vacancy conduction

Posted Date: June 16th, 2021

DOI: <https://doi.org/10.21203/rs.3.rs-357069/v1>

License:   This work is licensed under a Creative Commons Attribution 4.0 International License.

[Read Full License](#)

Version of Record: A version of this preprint was published at Journal of Materials Science: Materials in Electronics on August 3rd, 2021. See the published version at <https://doi.org/10.1007/s10854-021-06541-x>.

Abstract

The topotactic reduction of $\text{La}_{0.75}\text{Ba}_{0.10}\text{Sr}_{0.15}\text{FeO}_{2.875}$ with titanium metal leads to a new isostructural material of the composition $\text{La}_{0.75}\text{Ba}_{0.10}\text{Sr}_{0.15}\text{FeO}_{2.875-\delta}$ ($\delta = 0.375$ and 0.50). XRD analysis of phases confirms that the obtained compound adopts a brownmillerite-type structure. A slight distorted monoclinic $P2/m$ was found to describe the crystal structure. The transport properties have been investigated by current–voltage (I – V). The electric and dielectric measurements were carried out covering a wide range of temperature (300–600 K). Our materials display semiconducting properties as well as mixed ionic and electronic conductivity. At high temperatures, the activation energy values proved to be around 907 – 630 meV, which refers basically to oxygen vacancies conduction. The analysis of dielectric properties and dielectric losses (ϵ' , $\tan\delta$) of both compounds vs temperature at different frequencies demonstrates two relaxer attitudes. A low dielectric loss and low electrical conductance were displayed. Relying upon these values, these materials stand for perfect candidates for micro-electronics devices.

1. Introduction

Much ink has been spilled upon oxygen deficient perovskite oxides owing to their multiple merits [1]. Indeed, they exhibit a mixed ionic and electronic conductivity [2]. Besides, these ceramics are promising materials for a wide range of technological applications [3–7]. Moreover, ferroelectrics oxides are gaining much popularity in recent years in view of their high colossal dielectric constant ($\epsilon \approx 10^3$) [8]. This behavior has potential enhancements in microelectronics devices, such as random access memories and capacitors [9–11]. They are basically used in reducing of the size of electronic components such as capacitive components [12].

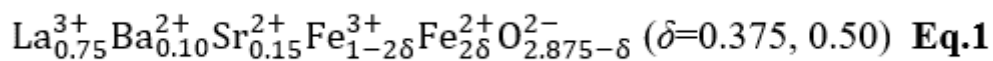
In $\text{ABO}_{3-\delta}$ perovskites, B-site cations conventionally create BO_6 , BO_5 , or BO_4 polyhedral depending on the structure. Their crystal structure depends largely on the arrangement of defects generated from oxygen vacancy creation. These defects can follow a disordered or ordered pattern [13, 14] leading to a new material. One of the common structures resulting from oxygen ordering is brownmillerite type structure with $\text{A}_2\text{B}'\text{O}_5$ formula. In a typical brownmillerite, the octahedral B and tetrahedral B' sites are exhibited in layers parallel to the long axis. The brownmillerite structure can be derived from the cubic phase by removing 1/6 of all oxygen atoms ordered in the pseudocubic direction $[110]$ [5][15–17]. Previous studies reported [18, 19] that the brownmillerite structure with composition $\text{A}_2\text{B}_2\text{O}_5$, remains ambiguous between Pnma , Imma , C2/c and I2mb space group owing to different orientations of tetrahedral chains with respect to each other.

This structural change leads to the enhancement of electric and dielectric properties of these materials presenting ionic and electronic conductivity [2].

Previously, oxygen deficient perovskites could be formed through quenching the perovskite from high temperature to room temperature [20] or using a forming gas of H_2 in Ar [21]. In this work, our central focus is upon a new method to create nontoxic, low costed and simply processed multiferroic samples.

In our previous papers [22], we confined our study to the oxygen deficient samples $\text{La}_{0.75}\text{Ba}_{0.10}\text{Sr}_{0.15}\text{FeO}_{2.875-\delta}$ for deficiency rates less than 0.25. In order to extend this work and build upon it, we attempted to increase the deficiency oxygen concentration so as to investigate their effect on the purity of phases (to examine the degree of non-stoichiometry to which the perovskite structure is presented). In our laboratories and for the first time, we have successfully elaborated perovskite deficient oxygen samples with a rate higher than 0.25. The basic objective of this research paper lies in investigating the structure as well as electric and dielectric properties of samples.

In order to maintain overall electrical neutrality and owing to the creation of oxygen vacancies, the amounts (2δ) of Fe^{3+} are reduced by (2δ) Fe^{2+} cations. The developed electronic formula of these materials is expressed in terms of



2. Experimental Details

Our samples were obtained from an already made perovskite $\text{La}_{0.75}\text{Ba}_{0.10}\text{Sr}_{0.15}\text{FeO}_{2.875}$, which was synthesized via sol gel method followed by thermal active process using oxygen acceptor metal (titanium Ti). This procedure was well described in our previous work [22]. Following the same procedure, we prepared the samples with $\delta = 0.375$ and $\delta = 0.50$.

Phase identification was undertaken through powder X-ray diffraction (XRD), where data were collected by Burker 8D Advance X-ray powder diffractometer with CuK α radiation ($\lambda = 0.15406$ nm) in steps of 0.02° for $10^\circ \leq 2\theta \leq 100^\circ$. A structure refinement was carried out using the Rietveld method. The scanning electron microscopy (SEM) observations and compositional analysis were recorded using TESCAN VEGA3 SBH equipped with an energy dispersive X-ray system (EDX). To determine the different vibrational bands, the Fourier transform infrared (FTIR) spectra were specified in the wavenumber range $550\text{--}1000\text{ cm}^{-1}$, using a Perkin Elmer spectrometer. The spectra were elaborated at room temperature. The current–voltage (I–V) measurements were set forward using a voltmeter (Agilent 34,401) and a current source (Keithley 220). The impedance measurements were estimated on pellets with a diameter of 5 mm and 1.5 mm of thickness on using an Agilent 4294A Precision Impedance Analyzer and cold plate of a liquid nitrogen cooled cryostat to measure the capacitance and conductance over a wide frequency and temperature range.

3. Results And Discussion

3.1. X-ray diffraction and morphological characterization

Room-temperature XRD data collected from the as-prepared samples with $\delta = 0.375$ and $\delta = 0.50$ are depicted in Fig. 1(a). The crystallographic study demonstrated that those samples adopt the brownmillerite-type structure with no traces of secondary phase. A structural transition from orthorhombic structure (Pnma) with the splitting of peaks can be observed on X-ray diffraction spectra. The structural transition appears for $\delta = 0.375$ and $\delta = 0.5$ corresponding to an Fe^{2+} concentration between 75 % and 100 %. As the amount of oxygen deficiency increases, the intensities of peaks decrease, as revealed with the most intense peak in Fig. 1(a).

The profile refinement was carried out using the Fullprof software [23] and the pseudo-Voigt functions were invested for peak profile fitting. The refined lattice parameters and the discrepancy factors are exhibited in Table. 1. The R_p and R_{Wp} factors displayed much higher values than expected, which is accounted for in terms of the peaks with small intensities [21]. The difference between the fitted and experimental intensities of the reflection peaks may be assigned to preferred orientation effects [23, 24].

Figure 1(b) and 1(c) characterizes the Rietveld refinement taking into account the sample with $\delta = 0.50$. The reflection peaks were crystallized in the monoclinic system with P2/m space group. The average crystallite size was determined by well-known Scherer equation [25] and the results are outlined in Table. 1.

The elemental composition of the compound was measured by Energy dispersive X-ray analysis. EDX spectrum (Fig. 2) unveils the presence of characteristic peaks of La, Ba, Sr, Fe and O elements integrated during the preparation. The inset of the Fig. 2 illustrate the room temperature SEM micrographs of the $\text{La}_{0.75}\text{Ba}_{0.10}\text{Sr}_{0.15}\text{FeO}_{2.875-\delta}$ ($\delta = 0.375$ and 0.50) sample. These images show unique chemical contrast corresponding to the ferrite phase. The polycrystalline nature of the samples was confirmed from the existence of a large number of grains and grain boundaries in the samples.

A large distribution of grains was detected in SEM micrograph. Polygonal shape grains of varying sizes were observed for all the composition.

3.2. FTIR characterization

The crystal structure of the perovskite was identified through Fourier transform infrared (FTIR) spectra highlighting its characteristic absorption bands [26]. Figure 3 presents the FT-IR spectrum measured at room temperature in the frequency range of $550\text{--}1000\text{ cm}^{-1}$. The different vibration frequencies below 1000 cm^{-1} are assigned to the metal-oxygen vibrations bands owing to the strong affinity of bonding in metal oxide linkages. The vibrational band present at 750 cm^{-1} is attributed to the Fe-O-H bending vibrations [27]. The small peaks at around 850 cm^{-1} are indicative of the presence of metal oxide-bonds, which are assigned to the vibrations of Fe-O and O-Fe-O Bonds [27].

The vibration recorded at 900 cm^{-1} can be attributed to C-H bending vibrations [28].

For both samples, the spectra exhibit two bands characteristics of the metal cations' stretching vibrations inside the tetrahedral and octahedral sites. The FTIR spectra of the above mentioned samples display two main absorption bands corresponding to the vibrations of tetrahedral and octahedral site complexes [29]. The stretching vibration of the tetrahedral site lies in the wave-number range $550\text{--}800\text{ cm}^{-1}$ and the low frequency band below 550 cm^{-1} is assigned to the stretching vibrations of octahedral complexes.

The absorption band corresponding to the tetrahedral complexes composed of several sub-bands, are marked in Fig. 3 with ν (1) being centered at $\sim 750\text{ cm}^{-1}$, ν (2) at $\sim 680\text{ cm}^{-1}$, ν (3) at $\sim 630\text{ cm}^{-1}$, ν (4) at $\sim 610\text{ cm}^{-1}$, ν (5) at $\sim 580\text{ cm}^{-1}$ and ν (6) at $\sim 560\text{ cm}^{-1}$. The existence of sub-bands is suggestive of the presence of Fe^{2+} ions in ferrite structure [30–32], which is basically assigned to the Jahn-Teller distortion produced by the Fe^{2+} ions. This observation goes in good agreement with the observation noted by Rathod on Li-Zn ferrites [33].

Referring to pervious state of art works, the origin of the splitting of the main absorption band is not well processed. However, this can be inferred through the complex vibrations of the tetrahedral complexes which are highly correlated to the octahedral site complexes.

3.3. Current-voltage analysis

Before discussing dielectric properties, the current-voltage characteristic (I - V) was undertaken in order to test the contact quality. Figure 4 portrays (I - V) and (J - V) (where J is the current density) variations for both structures recorded under different temperatures. The I - V curves exhibit two symmetric fragments of lines. This behavior confirms the presence of no depletion layer [34]. In other words, the electrons can drift between the two electrodes without being reduced by depletion layer. As a matter of fact, we infer that the contact is of ohmic type. This attitude was also confirmed by the linear variation of double log-log I - V variation. The log-log plots of I vs V is fitted with the relation $I \propto V^n$, where n is found to be equal to 1 (ohmic relation between current-voltage).

3.4. Electrical conductance analysis

Most of the brownmillerite compounds [2], where the total conductivity includes the contribution of electronic and ionic conductivity, stand for mixed conductors. Our compounds possess the contribution of both electron and oxide-ion conductivity in view of the presence of oxygen vacancies and mixed valence states of iron ions ($\text{Fe}^{2+}/\text{Fe}^{3+}$) [35].

The electrical conductance investigation over a wide temperature (300–620 K) and frequency ($40\text{--}10^6$ Hz) ranging for $\delta = 0.375$ and 0.50 samples are illustrated in Fig. 5(a). This entity is indicated by the relation [36]

$$G = \sigma \frac{A}{l} \quad \text{Eq. 2,}$$

where σ is the conductivity, A is cross sectional area of material and l is its length.

The conduction is ensured by the hopping of electron from Fe^{3+} to Fe^{2+} ions and the presence of oxygen vacancy [35]. The increase in temperature enhances the hopping phenomenon resulting in an increase in the conduction process and therefore leading to the conductance increase [37].

The frequency dependence of conductance is examined by Jonscher's law [38, 39]

$$G = G_{dc} + G_{ac} = G_{dc} + A\omega^s \text{ Eq. 3}$$

Referring to the expression stated above, G_{dc} and G_{ac} represent the conductance in continuous and alternative current, respectively. A is a pre-exponential factor dependent on temperature, ω is the angular frequency and s is the frequency exponent ($0 \leq s \leq 1$).

We can infer from the conductance measurements that for each temperature, the spectrum can be divided into two parts. A Plateau appears at low frequencies (frequency independent conductance (40 Hz to 10^3 Hz)) attributed to dc-conductance bulk. The low-frequency plateau gets larger proportionally to the increase of temperature. The second part corresponds to the higher frequency dispersion region. This part corresponds to ac-conductance [40].

The experimental conductance data were fitted by **Eq. 3** for the investigated samples. A typical example of this fitting at $T = 500$ K is illustrated in Fig. 5(b) (red solid line). A close agreement is traced between the experimental data and the fitted one. As noticed, the conductance decreases with the increase in δ rate. Departing from the electronic neutrality of $\delta = 0.375$ (25% Fe^{3+} , 75% Fe^{2+}) and $\delta = 0.50$ (100% Fe^{2+}) compounds, we detect that the oxygen deficiency reduces the $\text{Fe}^{2+}/\text{Fe}^{3+}$ ratio. Thus, the number of hopping sites decreases. The presence of oxygen vacancy is responsible for the excess of Fe^{2+} ions over Fe^{3+} ions.

DC conductance findings resulting from conductance measurements at low frequencies are portrayed in Fig. 6(a) for both studied compounds. The activation energy values E_a corresponding to G_{dc} were estimated from the Arrhenius law as described by the following expression [41]

$$G_{dc} = A_0 \exp(-E_a/K_B T) \text{ Eq. 4,}$$

where A_0 is the pre-exponential factor, E_a is the activation energy and K_B is the Boltzmann constant.

In view of the creation of oxygen defects (vacancies), a wide variation of conductivity is noticed. In addition to the three straight lines observed in the whole explored temperature range 300–620 K, we detect an interior region representing the plateau (as portrayed in Fig. 6(b)). Each one corresponds to a particular E_a which rises up proportionally to the corresponding temperature. The estimated values of E_a were highlighted in **Table. 2**. The determined values are very close to those previously obtained in oxygen vacancy ferroelectrics compounds [42].

The activation energy proves to be around 908 meV – 630 meV at high temperature (region VI). This finding can be assigned to the bigger charge than that of an electron. In other words, oxygen vacancies motion is the main responsible factor for conduction at high temperature [43, 44]. Relying upon other reports [45], the E_a of oxygen vacancy is around 1 eV. For region (II), the E_a attitude refers primarily to octahedral distortion obtained after oxygen vacancy creation [42]. The activation energy of low-temperature region (I) is attributed to the hopping process.

In region (III), we notice a metallic behavior confirming the existence of two charge carriers. Indeed, as temperature increases, the free electrons density increases as well. This enhances collision frequency between charge carriers and induces metallic behavior. At higher temperature, ion conduction appears and becomes predominant.

The creation of oxygen vacancies gives rise to additional properties of the compounds.

3.5. Permittivity analysis

The variation of dielectric (Fig. 7) constant with frequency demonstrates a normal behavior of polar dielectric materials [46] with giant constant (in the range of 10^4 at low frequency for $\delta = 0.375$ sample) and shows that it is temperature dependent. This colossal dielectric constant is mainly assigned to interfacial polarization ameliorated after oxygen vacancy creation [11]. The value of ϵ' decreases when frequency increases until it slowly reaches a constant value at higher frequencies. The observed behavior can be explained by Maxwell-Wagner polarization [47, 48]. It is noticeable that the magnitude of ϵ' decreases heavily with the increase of the concentration of oxygen vacancy. The Giant value of dielectric constant is reported for $\text{La}_{0.75}\text{Ba}_{0.10}\text{Sr}_{0.15}\text{FeO}_{2.875-\delta}$ ($\delta = 0.375$) samples around 5.10^4 Fm^{-1} and about 300 Fm^{-1} for $\text{La}_{0.75}\text{Ba}_{0.10}\text{Sr}_{0.15}\text{FeO}_{2.875-\delta}$ ($\delta = 0.50$) samples. The probably explanation is the decrease of the number of dipoles sharing in the polarization process.

Moreover this decrease can be explained by an increase in FeO_6 titling due to the insertion of oxygen vacancy [11].

The thermal variation of dielectric properties are examined at different frequencies (10^3 , 10^4 , 10^5 and 10^6 Hz) in Fig. 8. Two dielectric relaxations are observed. These dielectric peaks are seen around 500 K and 620 K for all frequencies. This critical temperature is known as transition temperature. The charge carriers hopping between Fe^{3+} and Fe^{2+} ions play the main role behind the dielectric relaxation at low temperature. Furthermore, the low temperature peak may refer to the transition from ferroelectric to anti-ferroelectric state.

However, at high temperature, the dielectric relaxation is associated with oxygen vacancy and the peak corresponds to the transition from anti-ferroelectric state to paraelectric state.

The sample displays a peaking behavior at a specific temperature, owing to the jumping frequency of an electron between Fe^{3+} and Fe^{2+} , which becomes equal to the applied field frequency at this specific

temperature. In fact, when both frequencies are the same, the polarization increases gradually until reaching its maximum. Then, the applied frequency keeps increasing while the other one can't maintain this rise. This leads eventually to polarization decreasing. Thus, the dielectric constant decreases. Yet, this evolution can be assigned to intrinsic effects [11]. The oxygen vacancy creation increases the coulombic repulsive force between iron ions. When samples are exposed to an ac electric field, the iron ions can be displaced around without distorting the octahedral FeO_6 . From this perspective, this effect proves to be the cause of the increase in the dielectric constant proportional to the temperature.

The loss factor variation (Fig. 9) indicates a very similar trend as the dielectric constant exhibits two relaxer behaviors at low and high temperature. As reported in Fig. 9, the oxygen vacancy decreases the dielectric loss leading to a better use in future applications [8]. The decrease of dielectric loss with oxygen vacancy concentration is associated with the decrease of electrical conductance.

4. Conclusion

This research paper presents an overview of structural, electrical and dielectric investigation of oxygen deficient perovskites. Samples with chemical compositions $\text{La}_{0.75}\text{Ba}_{0.10}\text{Sr}_{0.15}\text{FeO}_{2.875-\delta}$ ($\delta = 0.375$ and 0.50) confirm the brownmillerite-type structure. The compounds crystallize in the monoclinic system with $P2_1/m$ space group. Conductance plots reveal the electrical properties as a function of temperature (300–600 K) and frequency 40– 10^6 Hz. A semiconducting behavior is recorded with the important contribution of ionic conductance to the total conductance (electron and holes electron). The activation energy at high temperature is basically assigned to the oxygen vacancy. The study of dielectric properties (ϵ' , $\tan\delta$) of both compounds vs temperatures at different frequencies characterizes two relaxer attitudes. At this stage of analysis, we would assert that our materials prove to be a promising candidate for different micro electric devices thanks to their low dielectric loss as well as low conductance.

Declarations

Competing interests: The authors declare no competing interests.

References

1. S.V. Chernov, Y.A. Dobrovolsky, S.Ya Istomin, E.V. Antipov, J. Grins, G. Svensson, N.V. Tarakina, A.M. Abakumov, G. Van Tendeloo, S.G. Eriksson, M.H. Seikh, Rahman, "Sr₂GaScO₅, Sr₁₀Ga₆Sc₄O₂₅, and SrGa_{0.75}Sc_{0.25}O_{2.5}: a Play in the Octahedra to Tetrahedra Ratio in Oxygen-Deficient Perovskites". *J. Inorg chem.* **51**, 1094–1103 (2012)
2. R.K. Hona, A. Huq, F. Ramezanipour, "Electrical properties of the ordered oxygen-deficient perovskite Ca₂Fe_{0.5}Ga_{1.5}O₅", *J. Ionics.* **25** 1315–1321 (2019)
3. W.G. Wang, M.B. Mogensen, "High-performance lanthanum-ferrite-based cathode for SOFC", *J. Solid. State. Ion.* **176** 457 – 462 (2005)

4. S. Chunwen, H. Rob, R. Justin, "Cathode Materials for Solid Oxide Fuel Cells: A Review", *J. Solid. State. Electr.* **14** 1125–1144 (2010)
5. M. Ceretti, S. Corallini, W. Paulus, Influence of Phase Transformations on Crystal Growth of Stoichiometric Brownmillerite Oxides: $\text{Sr}_2\text{ScGaO}_5$ and $\text{Ca}_2\text{Fe}_2\text{O}_5$, *J. Crystals.* **6** 146 (2016)
6. G. Chen, W. Zhou, D. Guan, J. Sunarso, Y. Zhu, X. Hu, W. Zhang, Z. Shao, "Two orders of magnitude enhancement in oxygen evolution reactivity on amorphous $\text{Ba}_{0.5}\text{Sr}_{0.5}\text{Co}_{0.8}\text{Fe}_{0.2}\text{O}_{3-\delta}$ nanofilms with tunable oxidation state", *J.Sci. Adv.* **3**(6) e1603206 (2017)
7. L. Gómez, V. Galean, R. Parra, CR. Michel, C. Paucar, O. Morán, "Carbon dioxide gas sensing properties of ordered oxygen deficient perovskite $\text{LnBaCo}_2\text{O}_{5+\delta}$ (Ln = La, Eu)", *J. Sens. Actuator B-Chem.* **221** 1455–1460 (2015)
8. P. Lunkenheimer, V. Bobnar, A.V. Pronin, A.I. Ritus, A.A. Volkov, A. Loidl, Origin of apparent colossal dielectric constants, *J. Phys. Rev B.* **66** 052105 (2002)
9. S. Saha, T. P. Sinha, "Dielectric relaxation in $\text{SrFe}_{1/2}\text{Nb}_{1/2}\text{O}_3$ ", *J. Appl. Phys.* **99** 014109 (2006)
10. A. Mishra, S.N. Choudhary, K. Prasad, R.N.P. Choudhary, Complex impedance spectroscopic studies of $\text{Ba}(\text{Pr}_{1/2}\text{Ta}_{1/2})\text{O}_3$ ceramic, *J. Physica B.* **406** 3279–3284 (2011)
11. W. Hzez, H. Rahmouni, E. Dhahri, K. Khirouni, "Dielectric properties of niobium-based oxide", *J.Alloy. Compd.* **725** 342–348 (2017)
12. W. Hzez, A. Benali, H. Rahmouni, E. Dhahri, K. Khirouni, B.F.O. Costa, "Effects of oxygen deficiency on the transport and dielectric properties of NdSrNbO ", *J. Phys. Chem. Solids.* **117** 1–12 (2018)
13. F. Ramezanipour, JE. Greedan, J. Siewenie, RL Donaberger, S. Turner, GA. Bottong, "A vacancy-disordered, oxygen-deficient perovskite with long-range magnetic ordering: local and average structures and magnetic properties of $\text{Sr}_2\text{Fe}_{1.5}\text{Cr}_{0.5}\text{O}_5$ ", *J. Inorg. Chem.* **51** 2638–2644 (2012)
14. R.K. Hona, A. Huq, F. Ramezanipour, "Magnetic structure of $\text{CaSrFeCoO}_{6-\delta}$: correlations with structural order", *J. Mater. Res. Bull.* **106** 131–136 (2018)
15. J. Young, J.M. Rondinelli, "Crystal structure and electronic properties of bulk and thin film brownmillerite oxides", *J. Phys. Rev. B.* **92** 174111 (2015)
16. C. Mitra, T. Meyer, H.N. Lee, F.A. Reborado, "Oxygen diffusion pathways in brownmillerite $\text{SrCoO}_{2.5}$: influence of structure and chemical potential", *J. Chem. Phys.* **141** 084710 (2014)
17. X.Z., H.M. Zhai, W.L. Deng, P.X. Zhou, J.H. Yang Chu and Z.Zheng, "Structural, optical and magnetic tunability in KBiFe_2O_5 multiferroics", *J. RSC. Adv.* **5** 82351–82356 (2015)
18. T. G. Parsons, H. D'Hondt, J. Hadermann, M. A. Hayward, "Synthesis and Structural Characterization of $\text{La}_{1-x}\text{AxMnO}_{2.5}$ (A = Ba, Sr, Ca) Phases: Mapping the Variants of the Brownmillerite Structure", *J. Chem. Mater.* **21** 5527–5538 (2009)
19. C. Greaves, A. J. Jacobson, B. C. Tofield, B. E. F. Fender, "A powder neutron diffraction investigation of the nuclear and magnetic structure of $\text{Sr}_2\text{Fe}_2\text{O}_5$ ", *J. Acta. Cryst.* **31** 641–646 (1975)
20. Z. Zeng, M. Greenblatt, M. Croft, Large magnetoresistance in antiferromagnetic $\text{CaMnO}_{3-\delta}$, *J. Phys. Rev. B.* **59** 8784. (1999)

21. Jaemin Kim, Xi Yin, Kai-Chieh Tsao, Shaohua Fang, Hong Yang, "Ca₂Mn₂O₅ as Oxygen-Deficient Perovskite Electrocatalyst for Oxygen Evolution Reaction", *J. Am. Chem. Soc.* **136** 14646–14649 (2014)
22. M. Bouzayen, R. Dhahri, A. Benali, S. Chaabouni, K. Khirouni, B.F.O. Costa, Influence of oxygen deficiency on optical and dielectric properties of La_{0.75} Ba_{0.10} Sr_{0.15} FeO_{2.875-δ} compounds, *J. Chem. Phys. Lett.* 741 137106 (2020)
23. H.M. Rietveld, "A profile refinement method for nuclear and magnetic structures", *J. Appl. Cryst.* 2 65–71 (1969)
24. R. Bellouz, S. Kallel, K. Khirouni, O. Pena, M. Oumezzine, "Structural, Electrical conductance and complex impedance analysis of (Nd_{1-x}Ce_x)_{0.7}Sr_{0.3}MnO₃ (0 ≤ x ≤ 0.20) perovskite", *J. Ceram. In.* 41 1929–1936 (2015)
25. A. Taylor, *X. Metallography*, Wiley, New York, (1961)
26. A. Selmi, S. Hcini, H. Rahmouni, A. Omri, Mohamed Lamjed Bouazizi and Abdessalem Dhahri, "Synthesis, structural and complex impedance spectroscopy studies of Ni_{0.4}Co_{0.4}Mg_{0.2}Fe₂O₄ spinel ferrite", *J. Phase Transit.* 90 942–954 (2017)
27. F.B., A. Abdallah, M. Benali, E. Triki, K. Dhahri, G. Nomenyo, Lerondel, Investigation of structural, morphological, optical and electrical properties of double-doping Lanthanum ferrite, *J. Mater. Sci. Mater. Electron.* 30 3349–3358 (2019)
28. D. Bouokkeze, J. Massoudi, W. Hzez, M. Smari, A. Bougoffa, K. Khirouni, E. Dhahri, L. Bessais, Investigation of the structural, optical, elastic and electrical properties of spinel LiZn₂Fe₃O₈ nanoparticles annealed at two distinct temperatures, *J. RSC. Adv.* 9 40940–40955 (2019)
29. T.K. Pathak, J.J.U. Buch, U.N. Trivedi, H.H. Joshi, K.B. Modi, Infrared spectroscopy and elastic properties of nanocrystalline Mg–Mn ferrites prepared by co-precipitation technique, *J. Nanosci. Nanotechnol.* 8 4181–4187 (2008)
30. K. S. Aneesh Kumar and R. N. Bhowmik, "Micro-structural characterization and magnetic study of Ni_{1.5}Fe_{1.5}O₄ ferrite synthesized through coprecipitation route at different pH values", *J. Mater. Chem. Phys.* **146** 159–169 (2014)
31. S.A. Mazen, M.H. Abdallah, R.I. Nakhla, H.M. Zaki, "X-ray analysis and IR absorption spectra of Li-Ge ferrite", *J. Mater. Chem. Phys.* 34 35–40 (1993)
32. A.M. Shaikh, S.C. Watawe, S.A. Jadhav, B.K., Chougule, Preparation and characterization of Zn substituted Li–Mg ferrites, *J. Mater. Res. Bull.* 37 2547–2555 (2002)
33. V. Rathod, A.V. Anupama, R. Vijaya Kumar, V.M. Jali, B. Sahoo, Correlated vibrations of the tetrahedral and octahedral complexes and splitting of the absorption bands in FTIR spectra of Li-Zn ferrites, *J. Vib. Spectrosc.* 92 267–272 (2017)
34. A. Takshi, A. Dimopoulos, J.D. Madden, "Depletion width measurement in an organic Schottky contact using a metal-semiconductor field-effect transistor", *J. Appl. Phys. Lett.* **91** 1–3 (2007)

35. M. Bouzayen, R. Dhahri, A. Benali, S. Chaabouni, K. Khirouni, B. F.O. Costa," Synthesis and investigation of oxygen deficiency effect on electric properties of $\text{La}_{0.75}\text{Ba}_{0.10}\text{Sr}_{0.15}\text{FeO}_{2.875-\delta}$ ($\delta = 0.00, 0.125$ and 0.25) ferrites", *J. Mater. Sci: Mater. Electron.* 1–14 (2020)
36. M.E. Hajlaoui, R. Dhahri, N. Hnainia, A. Benchaabane, E. Dhahri, K. Khirouni," Conductivity and giant permittivity study of $\text{Zn}_{0.5}\text{Ni}_{0.5}\text{Fe}_2\text{O}_4$ spinel ferrite as a function of frequency and temperature", *J. RSC. Adv.* 9 32395–32402 (2019)
37. E. Oumezzine, S. Hcini, F.H.I. Rhouma, Mohamed Oumezzine,"Frequency and temperature dependence of conductance, impedance and electrical modulus studies of $\text{Ni}_{0.6}\text{Cu}_{0.4}\text{Fe}_2\text{O}_4$ spinel ferrite", *J. Alloy. Compd.* 726 187–194 (2017)
38. A.M., M.K. Abo El Ata, S.M. El Nimr, D. Attia, A.H. El Kony, Al-Hammadi, "Studies of AC electrical conductivity and initial magnetic permeability of rare-earth-substituted Li–Co ferrites", *J. Magn. Magn. Mater.* 297 33–43 (2006)
39. R. Tlili, M. Khelil, M. Bejar, M. Bekri, E. Dhahri, K. Khirouni, Role of gallium ion on the conducting properties of $\text{La}_{0.7}(\text{ba, sr})_{0.3}\text{Mn}_{1-x}\text{Ga}_x\text{O}_3$ ($x = 0.0, 0.1$ and 0.2) perovskite, *J. Ceram. Int.* 42 11256–11258 (2016)
40. M. Chebaane, N. Talbi, A. Dhahri, M. Oumezzine, K. Khirouni,"Structural and impedance spectroscopy properties of $\text{La}_{0.8}\text{Ba}_{0.1}\text{Ca}_{0.1}\text{Mn}_{1-x}\text{Ru}_x\text{O}_3$ perovskites", *J. Magn. Magn. Mater.* 407 334–340 (2016)
41. N. Hamdaoui, Y. Azizian-Kalandaragh, M. Khelifi, L. Beji,"Structural, magnetic and dielectric properties of $\text{Ni}_{0.6}\text{Mg}_{0.4}\text{Fe}_2\text{O}_4$ ferromagnetic ferrite prepared by sol gel method", *J. Ceram. Int.* **45** 16458–16465 (2019)
42. M.A. Wederni, S. Kraiem, R. Mnassri, H. Rahmouni, K. Khirouni," Ytterbium doping effects on structural, optical and electrical properties of $\text{Bi}_4\text{Ti}_3\text{O}_{12}$ system", *J. Ceram. Int.* **44** 21893–21901 (2018) [43] S. Zheng, D. Shi, L. Liu, G. Li, Q. Wang, L. Fang, B. Elouadi," Oxygen vacancy-related dielectric relaxation and electrical conductivity in La-doped $\text{Ba}(\text{Zr}_{0.9}\text{Ti}_{0.1})\text{O}_3$ ceramics", *J. Mater. Sci: Mater. Electron.* **25** 4058–4065 (2014)
43. Z. Raddaoui, R. Lahouli, S.E.L. Kossi, J. Dhahri, K. Khirouni, K. Taibi," Effect of oxygen vacancies on dielectric properties of $\text{Ba}_{(1-x)}\text{Nd}_{(2x/3)}\text{TiO}_3$ compounds", *J. Alloy. Compd.* 765 428–436 (2018)
44. J. Wang, X.G. Tang, H. L. W. Chan, and C. L. Choy,"Dielectric relaxation and electrical properties of $0.94\text{Pb}(\text{Fe}_{1/2}\text{Nb}_{1/2})\text{O}_3-0.06\text{PbTiO}_3$ single crystals", *J. Appl. Phys. Lett.* **86** 152907–152909 (2005)
45. S. Manzoor, Shahid Husain,"Influence of Zn doping on Structural, Optical and Dielectric Properties of LaFeO_3 ", *J. Mater. Res. Express.* 5 055009 (2018)
46. H.E.Sekrafi, A.Ben, Jazia Kharrat, M.A.Wederni, N.Chniba-Boudjada, K.Khirouni, W.Boujelben," Impact of low titanium concentration on the structural, electrical and dielectric properties of $\text{Pr}_{0.75}\text{Bi}_{0.05}\text{Sr}_{0.1}\text{Ba}_{0.1}\text{Mn}_{1-x}\text{Ti}_x\text{O}_3$ ($x = 0, 0.04$) compounds", *J. Mater. Sci.: Mater. Electron.* 30 876–891 (2019)
47. M. Idrees, M. Nadeem, M. Atif, M. Siddique, M. Mehmood, M.M. Hassan," Origin of colossal dielectric response in LaFeO_3 ", *J. Acta. Mater.* **59** 1338–1345 (2011)

Tables

e 1: the refinement parameters and crystallite size of $\text{La}_{0.75}\text{Ba}_{0.10}\text{Sr}_{0.15}\text{FeO}_{2.875-\delta}$ ($\delta = 0.375$ and 0.50).

Parameters	$\delta=0.375$	$\delta=0.50$
a (Å)	17.765 ₇	17.779
b (Å)	4.465	4.477 ₃
c (Å)	11.836 ₉	11.937 ₆
β (°)	118.459	118.505
V(Å ³)	825.479 ₃	835.064 ₅
Rp (%)	15.7	16.9
Rwp (%)	17.7	18.3
Rexp (%)	8.38	9.83
Dsc (nm)	42	41

e 2: Activation energy values of $\text{La}_{0.75}\text{Ba}_{0.10}\text{Sr}_{0.15}\text{FeO}_{2.875-\delta}$ ($\delta = 0.375$ and 0.50)
 ple.

Activation energy (meV)			
	Region I	Region II	Region IV
$\delta=0.375$	454	463	907
$\delta=0.50$	537	300	630

Figures

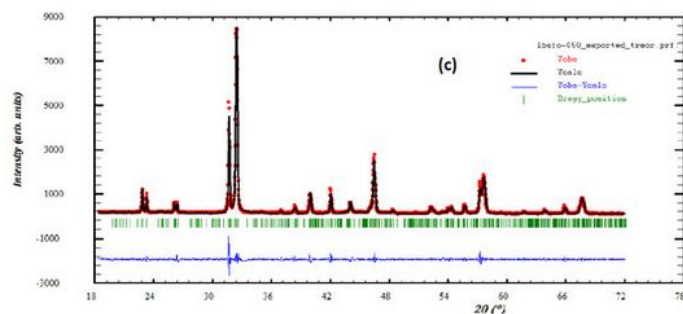
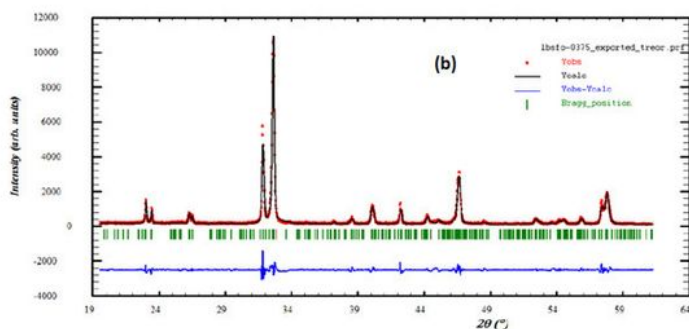
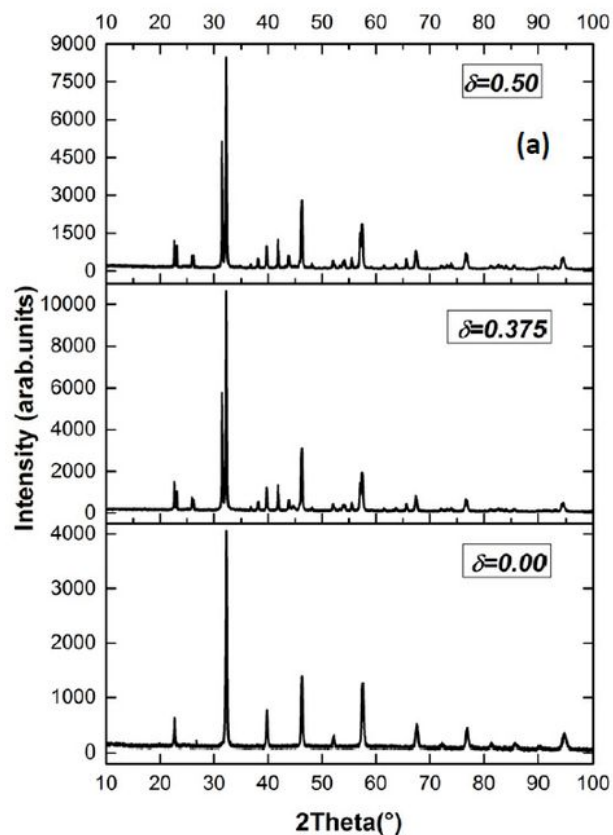


Figure 1

(a) X-ray diffraction pattern of $\text{La}_{0.75}\text{Ba}_{0.10}\text{Sr}_{0.15}\text{FeO}_{2.875-\delta}$ ($\delta = 0.00, 0.375$ and 0.50) (b): Measured (solid circles) and calculated (solid line) XRD patterns of $\text{La}_{0.75}\text{Ba}_{0.10}\text{Sr}_{0.15}\text{FeO}_{2.875-\delta}$ ($\delta = 0.375$ and 0.50) sample obtained at room temperature. The difference between these spectra is plotted at the bottom. Bragg reflections are indicated by ticks

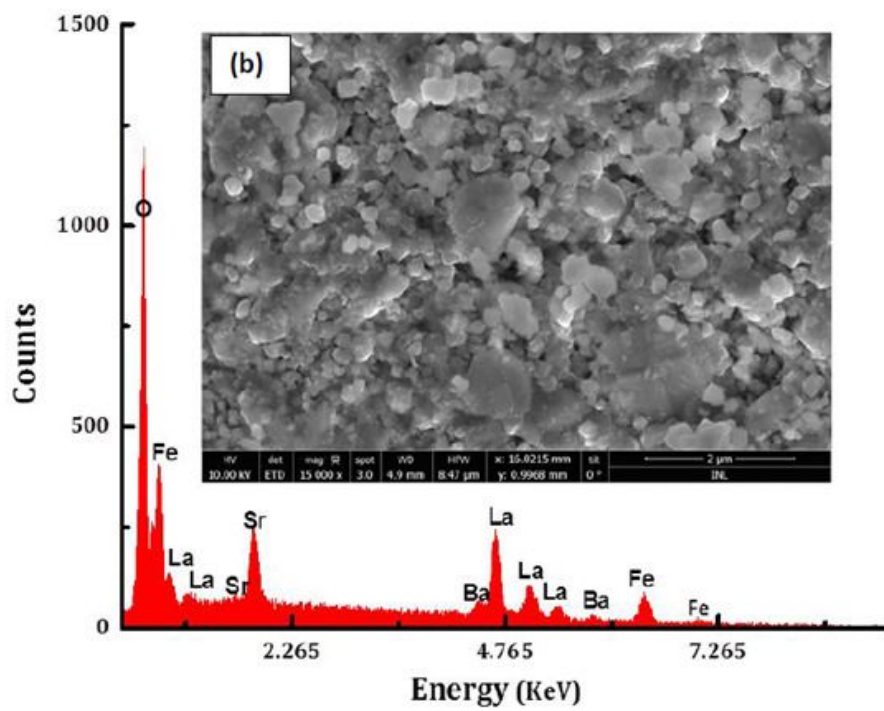
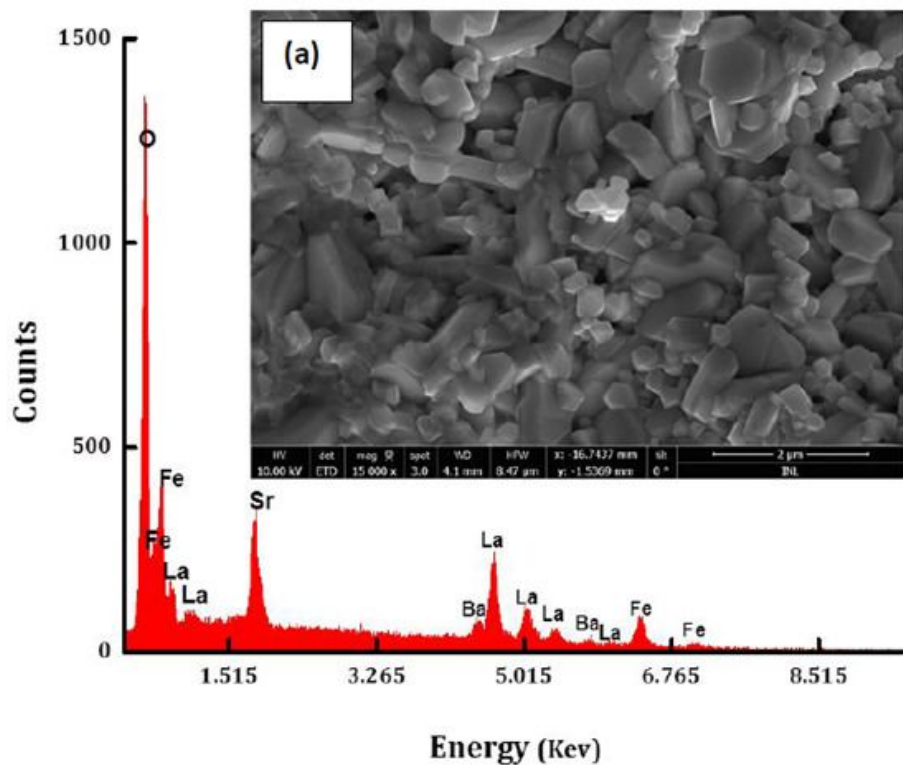


Figure 2

SEM micrographs and compositional analysis of $\text{La}_{0.75}\text{Ba}_{0.10}\text{Sr}_{0.15}\text{FeO}_{2.875-\delta}$ ($\delta = 0.375$ and 0.50)

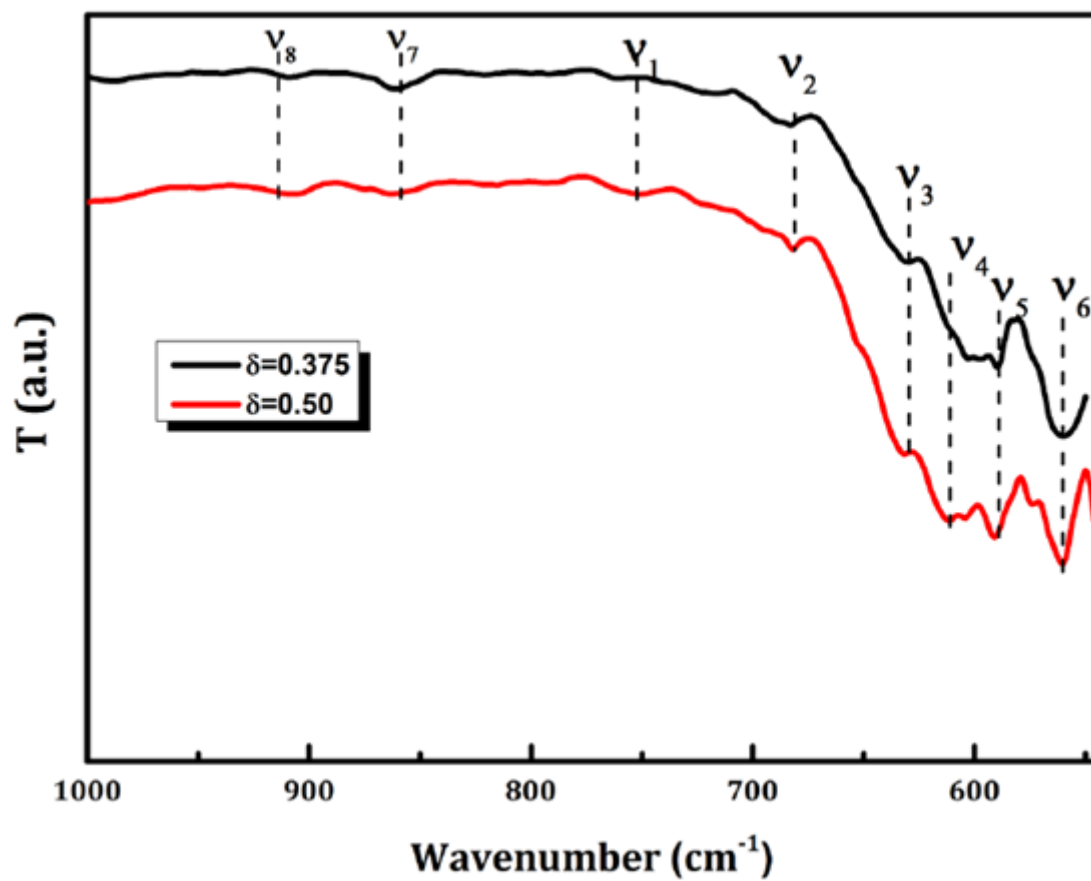


Figure 3

FTIR spectrum of $\text{La}_{0.75}\text{Ba}_{0.10}\text{Sr}_{0.15}\text{FeO}_{2.875-\delta}$ ($\delta = 0.375$ and 0.50)

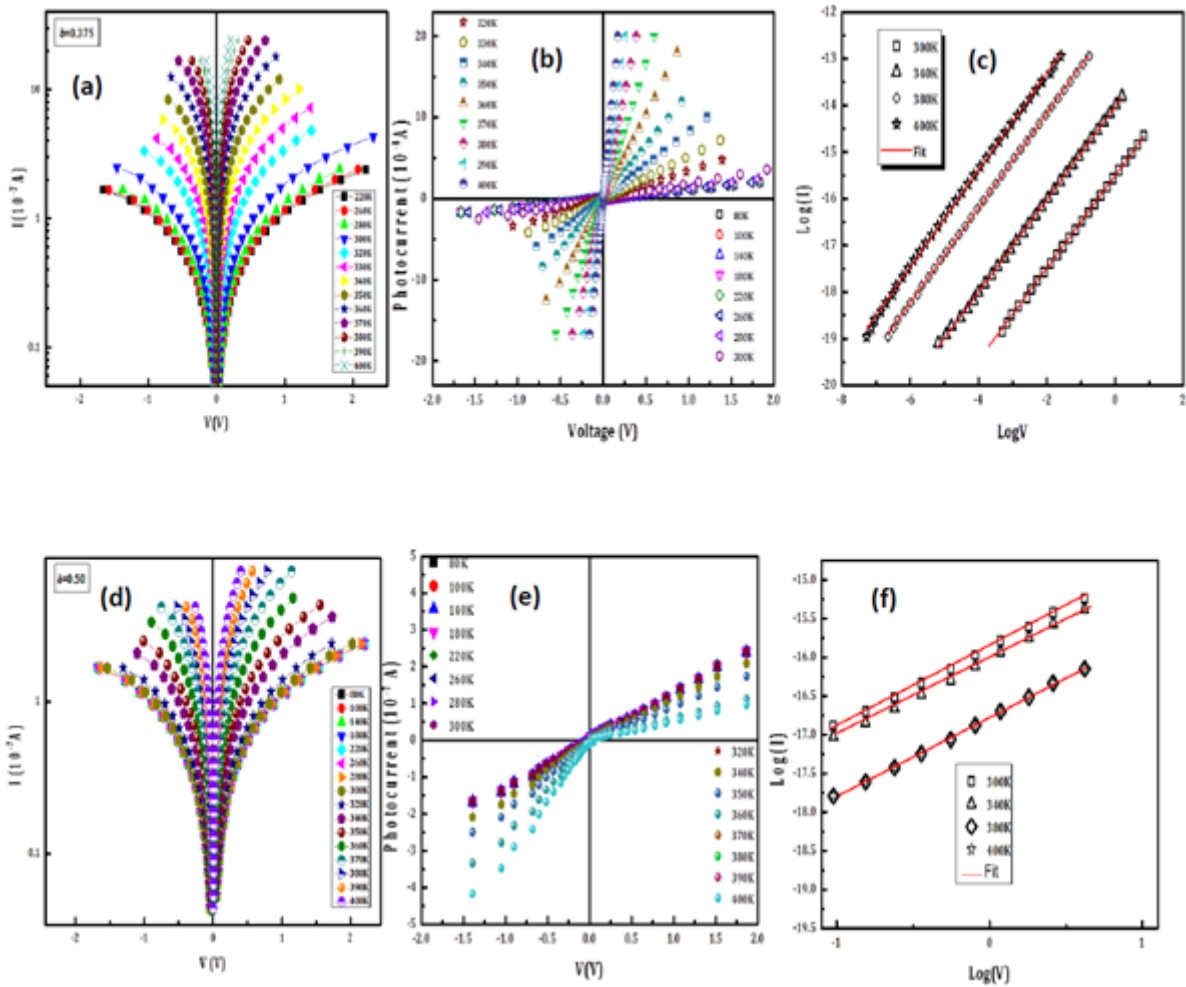


Figure 4

(a, b, c) Current vs Voltage characteristics, Current density vs Voltage and $\log(I)$ vs $\log(V)$ plot respectively for $\text{La}_{0.75}\text{Ba}_{0.10}\text{Sr}_{0.15}\text{FeO}_{2.875-\delta}$ ($\delta=0.375$) samples recorded at different temperatures. (d, e, f) Current vs Voltage characteristics, Current density vs Voltage and $\log(I)$ vs $\log(V)$ plot respectively for $\text{La}_{0.75}\text{Ba}_{0.10}\text{Sr}_{0.15}\text{FeO}_{2.875-\delta}$ ($\delta=0.50$) samples recorded at different temperatures.

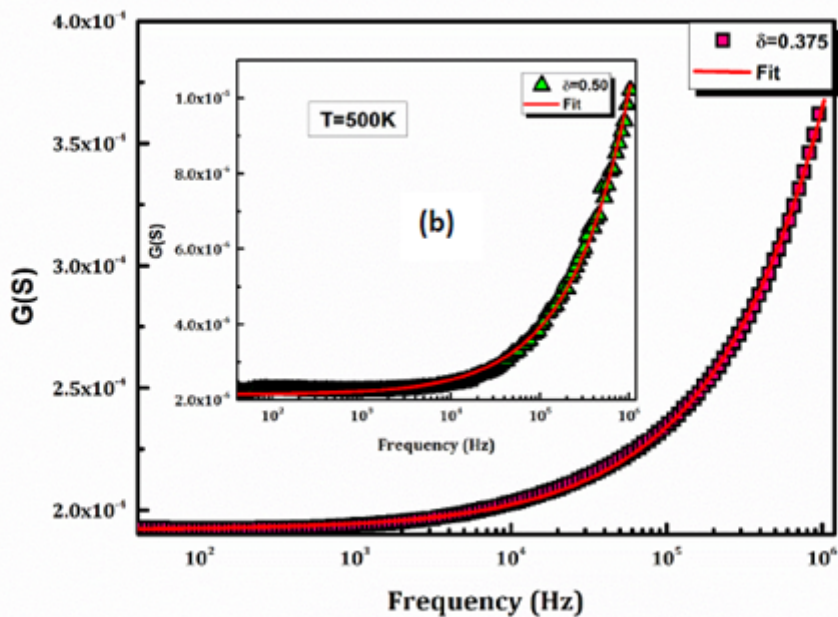
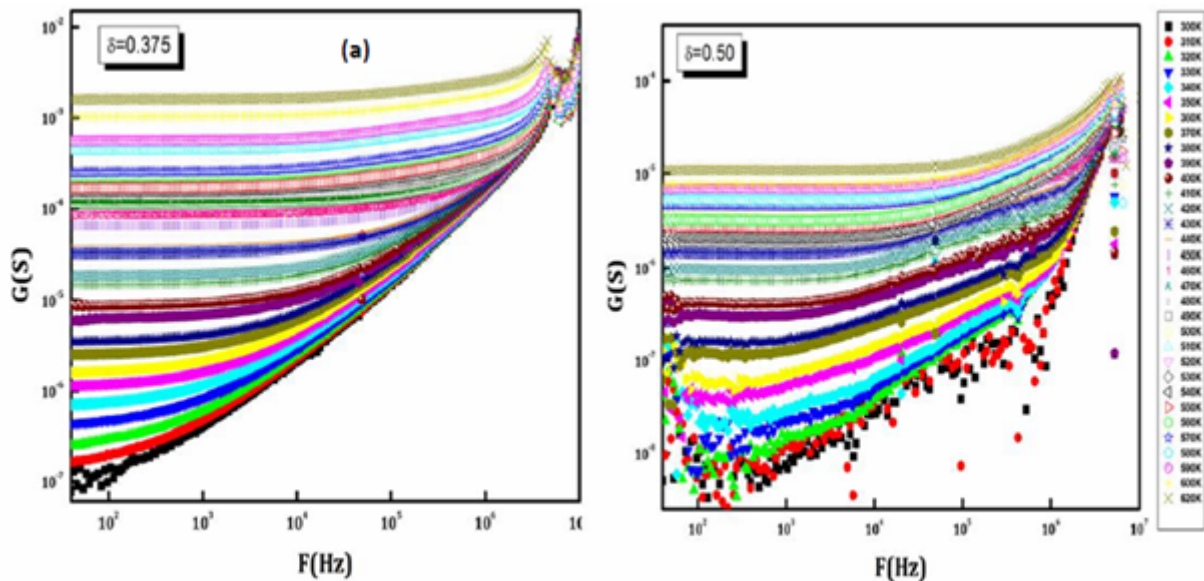


Figure 5

(a) Electrical conductance versus frequency at different Temperatures for $\text{La}_{0.75}\text{Ba}_{0.10}\text{Sr}_{0.15}\text{FeO}_{2.875-\delta}$ ($\delta=0.375$ and 0.50). (b) Red solid lines represent the fitting of the experimental data using the universal Jonscher's power law

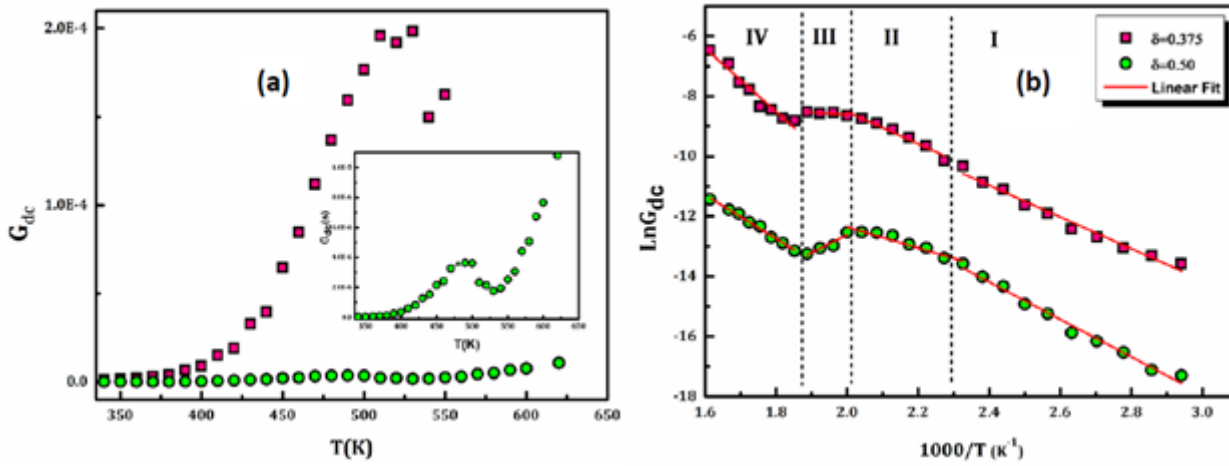


Figure 6

(a): The variation of dc-conductance with temperature (b): Variation of the $\ln(G_{dc})$ as a function of $1000/T$ for $\text{La}_{0.75}\text{Ba}_{0.10}\text{Sr}_{0.15}\text{FeO}_{2.875-\delta}$ ($\delta=0.375$ and 0.50) samples

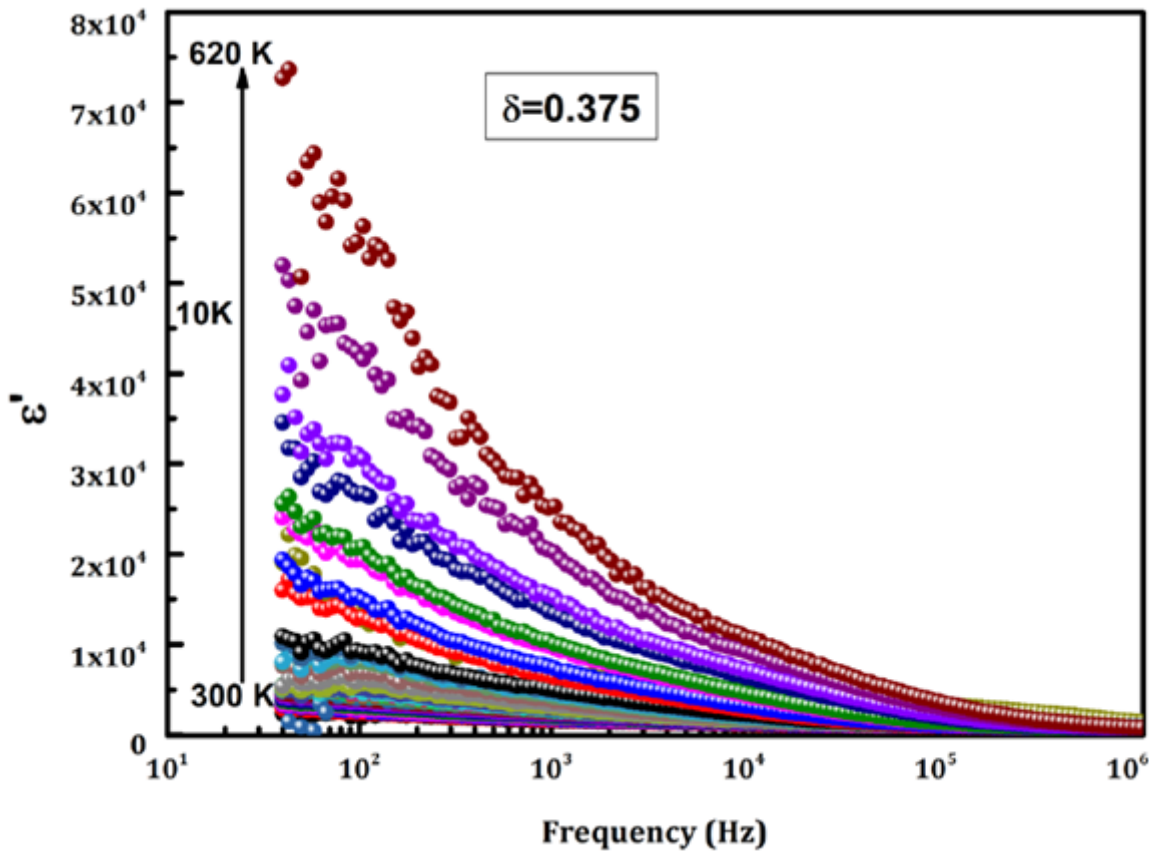


Figure 7

Variation of dielectric constant with frequency at different temperatures of $\text{La}_{0.75}\text{Ba}_{0.10}\text{Sr}_{0.15}\text{FeO}_{2.875-\delta}$ ($\delta=0.375$) samples

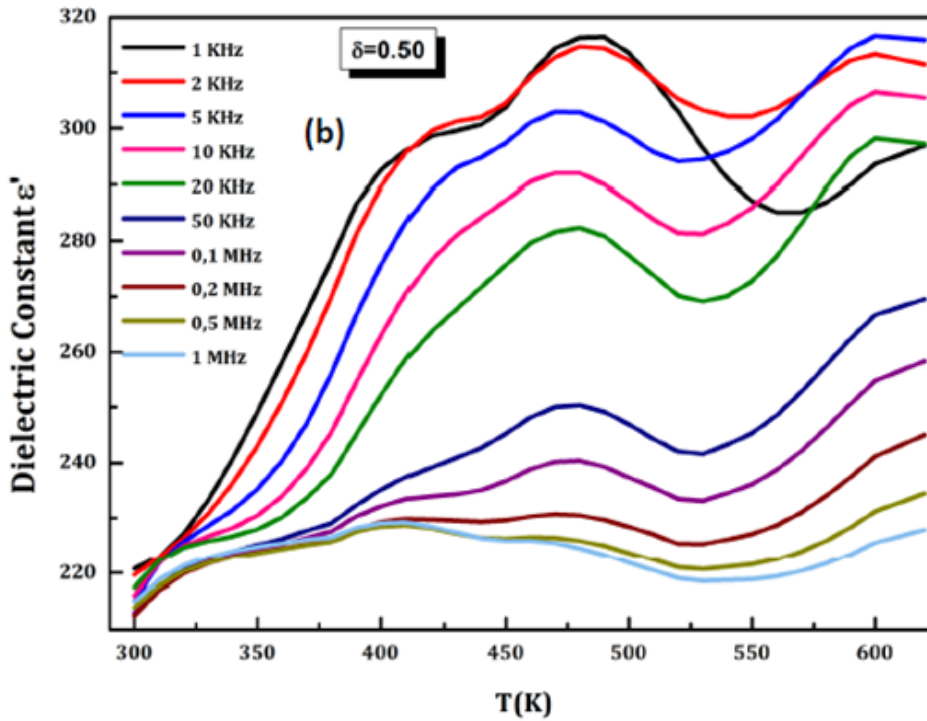
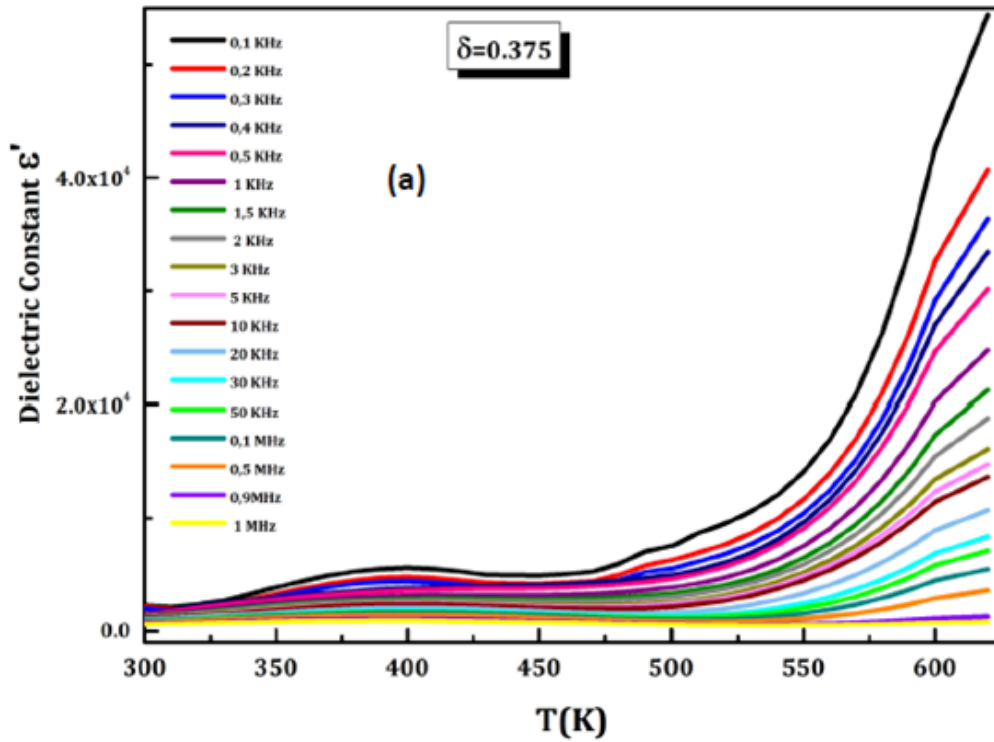


Figure 8

(a,b) Temperature dependence of real part of permittivity for $\text{La}_{0.75}\text{Ba}_{0.10}\text{Sr}_{0.15}\text{FeO}_{2.875-\delta}$ at different frequencies respectively for $\delta=0.375$ and 0.50

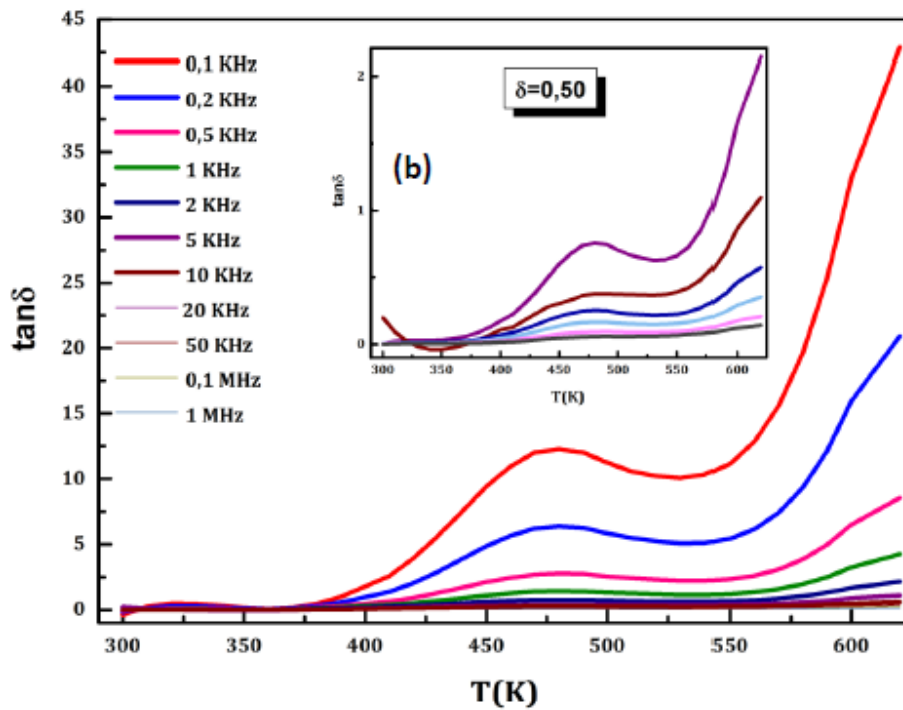
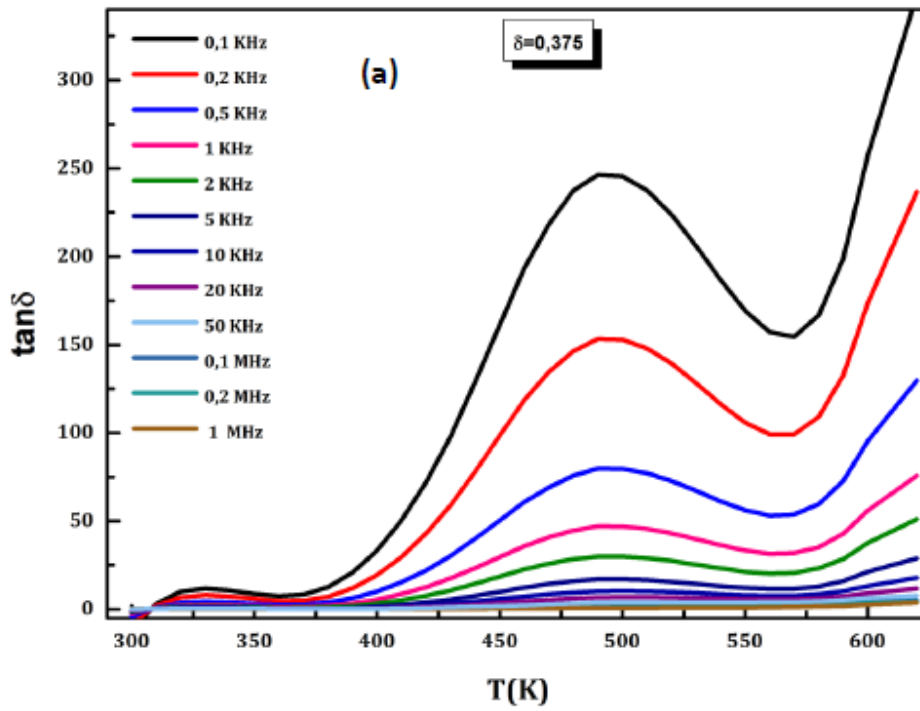


Figure 9

(a,b) Temperature dependence of loss factor of $\text{La}_{0.75}\text{Ba}_{0.10}\text{Sr}_{0.15}\text{FeO}_{2.875-\delta}$ at different frequencies respectively for $\delta=0.375$ and 0.50